Diagnosing Ozone-NO$_x$-VOCs-Aerosols Sensitivity and Uncovering Causes of Urban-Nonurban Discrepancies in Shandong, China using Transformer-Based Estimations

Chenliang Tao[1], Yanbo Peng[1,2,], Qingzhu Zhang[1,*], Yuqiang Zhang[1], Bing Gong[3], Qiao Wang[1], Wenxing Wang[1]*

[1]Big Data Research Center for Ecology and Environment, Environmental Research Institute, Shandong University, Qingdao 266237, P.R. China

[2]Shandong Academy for Environmental Planning, Jinan 250101, P.R. China

[3]Jülich Supercomputing Centre, Forschungszentrum Jülich, 52425 Jülich, Germany

Keywords:

Air pollution, Deep learning, Transformer, Satellite, Urban-rural difference, Ozone Regime

____

*Corresponding authors. E-mail: zqz@sdu.edu.cn, pengyanbo@mail.sdu.edu.cn

Abstract

Narrowing surface ozone disparities between urban and nonurban areas escalate health risks in densely populated urban zones. A comprehensive understanding of the impact of ozone photochemistry on this transition remains constrained by current knowledge of aerosol effects and the availability of surface monitoring. Here we reconstructed spatiotemporal gapless air quality concentrations using a novel Transformer deep learning (DL) framework capable of perceiving spatiotemporal dynamics to analyze ozone urban-nonurban differences. Subsequently, the photochemical effect on these discrepancies was analyzed by elucidating shifts in ozone regimes inferred from an interpretable machine learning method. The evaluations of model exhibited an average out-of-sample cross-validation coefficient of determination of 0.96, 0.92, and 0.95 for ozone, nitrogen dioxide, and fine particulate matter ($PM_{2.5}$), respectively. The ozone sensitivity in nonurban areas, dominated by nitrogen oxide (NO_x)-limited regime, was observed to shift towards increased sensitivity to volatile organic compounds (VOCs) when extended to urban areas. A third 'aerosol-inhibited' regime was identified in the Jiaodong Peninsula, where the uptake of hydroperoxyl radicals onto aerosols suppressed ozone production under low NO_x levels during summertime. The reduction of $PM_{2.5}$ would increase the sensitivity of ozone to VOCs, necessitating more stringent VOC emissions abatement for urban ozone mitigation. In 2020, urban ozone levels in Shandong surpassed those in nonurban areas, primarily due to a more pronounced decrease in the latter resulting from stronger aerosol suppression effects and lesser $PM_{2.5}$ reductions. This case study demonstrates the critical need for advanced spatially resolved models and interpretable analysis in tackling ozone pollution challenges.

1. INTRODUCTION

Surface ozone (O_3), fine particulate matter ($PM_{2.5}$), and nitrogen dioxide (NO_2) are among the most important trace gases in the atmosphere that significantly impact the ecological environment and public health (Han and Naeher, 2006; Yue et al., 2017). During the Action Plan on the Prevention and Control of Air Pollution (denoted as the Clean Air Action, 2013-2017) (Action Plan on Air Pollution Prevention and Control (in Chinese), 2023), $PM_{2.5}$ and nitrogen oxide (NO_x = nitric oxide (NO) + NO_2) emissions across China decreased by 33% and 21%, respectively (Zheng et al., 2018), while surface O_3 exhibited an increasing trend (Lu et al., 2018). The increase in O_3 could be partially attributed to the "aerosol-inhibited" effect, where the reduction in $PM_{2.5}$ results in a diminished reactive uptake of hydroperoxyl radicals (HO_2) onto aerosols (Ivatt et al., 2022; Li et al., 2019). The societal benefits of reducing premature deaths and economic losses from $PM_{2.5}$ reductions have been diminished by the rising O_3 (Liu et al., 2022). Thus, achieving the joint attainment objectives for $PM_{2.5}$ and O_3 has been put on the top priority of China's long-term air pollution control policies.

The complexity of the O_3 formation is partly reflected by the nonlinear response to changes in precursors (i.e. volatile organic compounds (VOCs) and NO_x), as well as the presence of heterogeneous reactions in aerosols. Understanding these dynamics is crucial to investigate current narrowing differences in O_3 concentrations between urban and nonurban areas, which have traditionally shown higher levels in rural (Han et al., 2023). The formaldehyde-to-NO_2 ratio ($HCHO/NO_2$ or FNR) serves as a theoretical

66 gauge of the relative abundance of total organic reactivity to hydroxyl radicals (OH)

67 and NO_x (Wei et al., 2022c; Sillman, 1995), and as such, it can function as a useful

68 indicator of O_3 sensitivity. Previous studies have utilized the $HCHO/NO_2$ from satellite

69 remote sensing to infer O_3 production regimes for guiding O_3 control policies (Jin et al.,

70 2023; Li et al., 2021a; Jin et al., 2020). However, the changes of $HCHO/NO_2$ threshold

71 in O_3 regimes classification modulated by meteorology and localized atmospheric

72 chemistry in space and time, and uncertainties relating column to surface, precluding

73 robust applications over larger spatial scales (Lee et al., 2023; Jin et al., 2017; Souri et

74 al., 2023). While the observation-based model method alleviates some of these

75 limitations, constraints remain including computational demands and priori chemical

76 mechanisms (Song et al., 2022b; Chu et al., 2023). The advent of interpretable machine

77 learning models affords new opportunities to unravel intricate dependencies governing

78 O_3 formation purely from actual observational data. However, sparse ground-based

79 monitoring stations, especially in rural areas, pose great challenges to the spatially full

80 coverage of studies. Thus, the high-spatiotemporal-resolutions estimations of surface

81 air pollutants are urgently needed to improve our understanding of how these pollutants

82 are changing and interacting.

83   Recent studies have utilized spatially resolved remote sensing data to estimate the

84 continuous distribution of air pollutants in space by diverse machine learning (ML)

85 models (Lyapustin and Wang, 2022; Lamsal et al., 2022; Huang et al., 2021; Li and

86 Wu, 2021; Ren et al., 2022b), such as random forest (RF), full residual deep learning,

87 and Bayesian ensemble model. These attempts have demonstrated the tremendous

88 potential of machine learning as an alternative to atmospheric chemical models (Jung

89 et al., 2022). Nevertheless, there are still several aspects that have not been fully

90 considered. For instance, coarse-resolution maps limit the ability to characterize the

91 fine-scale variation of air pollution within urban areas, which has significant

92 implications for environmental justice disparities of disadvantaged communities

93 (Jerrett et al., 2005; Ren et al., 2022b; Dias and Tchepel, 2018). Additionally, existing

94 ML models may not fully account for the complex atmospheric chemistry and physics

95 processes that influence pollutant concentrations due to the single-pixel-based

96 processing mode (Huang et al., 2021; Requia et al., 2020; Thongthammachart et al.,

97 2022; Li et al., 2022b; Geng et al., 2021). Although several efforts have been made by

98 using the neural network with convolutional layers (Di et al., 2016), and explicitly

99 incorporating spatiotemporally weighted information to machine learning models (Wei

100 et al., 2022b), the global spatiotemporal self-correlation of multi-dimensional features

101 in the input array remained unaddressed. Meanwhile, the convolutional operations

102 extract features from all neighboring grids of the target, ignoring the fact that the

103 environmental knowledge of the target grid itself is the most significant, with the

104 adjacent features being secondary.

105   In this study, we aim to analyze the evolving dynamics of urban-nonurban O_3

106 differences between 2019 and 2020. The roles of emission discrepancies and

107 nonlinearity of O_3-NO_x-VOCs-aerosols photochemical processes in shaping these O_3

108 variations were deeply dissected. To achieve a comprehensive analysis, we employed a

109 new spatiotemporal Transformer framework that paid special attention to air mass

110 transport and dispersion affected by the spatial-temporal correlations, to reconstruct the

111 spatially gapless air quality datasets based on satellite data, ground-level observations,

112 and meteorological reanalysis. The estimations are particularly vital for regions lacking

113 dense ground-based monitors, ensuring that our understanding of O_3 dynamics in urban-

114 nonurban areas and formation regimes is not limited by geographical constraints in data

115 availability. Surface O_3 formation regimes in Shandong province were inferred by the

116 classic XGBoost model (Chen and Guestrin, 2016) coupled with Shapley Additive

117 exPlanations (SHAP) (Lundberg and Lee, 2017), which identifies the impact of

118 meteorological conditions and photochemical indicators (i.e. $PM_{2.5}$ as a proxy for

119 aerosols, NO_2 as a proxy for NO_x, and HCHO as a proxy for VOCs) on O_3. The

120 innovative Transformer-based modeling and interpretable machine learning analysis

121 approaches are expected to enable new applications such as those of air quality

122 simulation and O_3 formation regimes studies.

123 2. MATERIALS AND METHODS

124 2.1 Predictor Variables

125   The study domain covered the Shandong province of China, which has a high

126 mortality burden of air pollution (Liu et al., 2017). The surface $PM_{2.5}$, O_3, and NO_2

127 concentration measurements were collected from the regulatory air quality stations of

128 the China National Environmental Monitoring Center (CNEMC, with a total of 179

129   locations) and the Shandong Provincial Eco-environmental Monitoring Center (SDEM,

130   with a total of 166 locations) (Fig. S1). The SDEM stations were included to fill the

131   spatial gaps in the county and rural areas where CNEMC stations were lacking. The

132   study area was divided into 1.22 million grid cells with a spatial resolution of 500

133   meters. We utilized a range of predictor data, including tropospheric NO_2 vertical

134   column densities (VCDs) and O_3 total VCDs measured by TROPOspheric Monitoring

135   Instrument (TROPOMI) (Lamsal et al., 2022; Copernicus Sentinel-5P (processed by

136   ESA), 2020), aerosol optical depth (AOD) data and atmospheric properties obtained

137   from Moderate Resolution Imaging Spectroradiometer (MODIS) Multi-Angle

138   Implementation of Atmospheric Correction products (Lyapustin and Wang, 2022),

139   AOD estimates from Modern-Era Retrospective Analysis for Research and

140   Applications as the supplement to MODIS (2015), meteorological reanalysis obtained

141   from the fifth generation atmospheric reanalysis dataset of European Centre for

142   Medium-Range Weather Forecasts (ECMWF) (ERA5) (Hersbach et al., 2023, p.5),

143   daily dynamic industrial emissions, moonlight-adjusted nighttime lights product

144   (Román et al., 2018), vegetation index (Didan, 2021), population density (WorldPop,

145   2018), road density, land use data (Jun et al., 2014), and the shuttle radar topography

146   mission digital elevation model. The detailed information for all predictive variables

147   is listed in Table S1 and discussed in Text S1-2. Taking space-variant and seasonal

148   patterns into consideration, several spatiotemporal indicators such as geographical

149   coordinates, Euclidean spherical coordinates, year, Julian date, and helix-shaped

150   trigonometric sequences, were also included as predictor variables (Text S3) (Sun et al.,

151   2022). Geographic Information Systems techniques, including reprojection and

152   resampling, were used to consolidate all the data obtained for consistent projection and

153   spatial scale. Finally, the Light Gradient Boosting Machine was used to fill satellite data

154   gaps (Text S4) (Ke et al., 2017).

155   **2.2 Air Transformer**

156   AiT is an individual Transformer model that adopts an encoder-decoder

157   architecture with multidimensional self-attention computation to dynamically capture

158   the spatiotemporal autocorrelation of atmospheric pollution changes from the

159   sequences of pixels and variables for more reliable spatial maps of estimation.

160   Compared with existing image and video recognition Transformers, such as ViT

161   (Dosovitskiy et al., 2021), Timesformer (Bertasius et al., 2021), and Uniformer (Li et

162   al., 2021b), AiT is innovative in incorporating self-attention across channels after the

163   pixels-based self-attention and taking advantage of the decoder. The former can capture

164   the correlations between predictor variables. The decoder was employed to enable

165   interaction between the primary target grid and neighboring grids. Predictor variables

166   with 8 timesteps within 1000 meters of the target grid cell were fed into the model to

167   learn spatiotemporally disparities among atmospheric pollutants for predicting O_3, NO_2

168   and $PM_{2.5}$ within the target grid point.

169   The overall architecture of the proposed AiT model and the dimensions of input

170   data are illustrated in Fig. 1. The encoder maps an input sequence with neighborhood

171   spatiotemporal data to a sequence with high-dimensional spatiotemporal characteristics,

172   and the decoder generates an estimation by computing self-attention representations

173   between the target grid and outputs of the encoder. The encoder of AiT takes as input a

174   clip $X \in R^{V \times T \times H \times W}$ consisting of T multi-variable frames of size $H \times W$ sampled

175   from the original dataset, where V is the number of variables and the target grid cell is

176   located at $(\lceil \frac{H}{2} \rceil, \lceil \frac{W}{2} \rceil)$. The decoder takes as input a clip $X \in R^{V \times 1 \times 1 \times 1}$ consisting of V

177   variables from the target grid. Several Transformer blocks with modified self-attention

178   computation (AiT blocks) are applied to the encoder. The AiT encoder block is similar

179   to the standard vision transformer block but specifically designed for atmospheric

180   estimation (Dosovitskiy et al., 2021). It is a stack of two self-attention schemes,

181   including global spatiotemporal self-attention on the pixels and channel self-attention

182   on variable predictors. The former contains $N = HW$ effective input sequence length

183   for the self-attention to extract spatiotemporal information. The latter computes self-

184   attention based on V effective input sequence length to capture hidden information on

185   variables. The decoder part is symmetric to the encoder part, but it only has a block

186   with the spatiotemporal self-attention mechanism. We compute the matrix of self-

187   attention outputs as:

$$Attention(Q, K, V) = \text{softmax}\left(\frac{QK^T}{\sqrt{d_k}} + \text{B} \right) \text{V} \qquad (1)$$

189   where Q, K, and V are the queries, keys, and values in the inputs of the particular

190   attention, respectively. d_k is the feature dimensionality of K, and B is the geographic

191   positional bias term. Another difference is that the attention function of the decoder is

192 computed on Q from the estimated grid data, and (K, V) from the outputs of encoder

193 blocks under the same stage, resulting in the outputs of the last decoder block being

194 sized 1 × 128. The description of the data transformation and design details in the

195 process of training can be found in Text S5. The multi-task learning strategy was also

196 applied for learning representation across multiple pollutant estimation tasks (Text S6).

197 The aggregated feature data from June 2019 to June 2021 were utilized to train and

198 validate the model through cross-validation (CV), where the optimal model, trained

199 based on out-of-sample CV, was used to estimate multiple pollutant concentrations

200 during the study period, which was then employed for subsequent analysis.
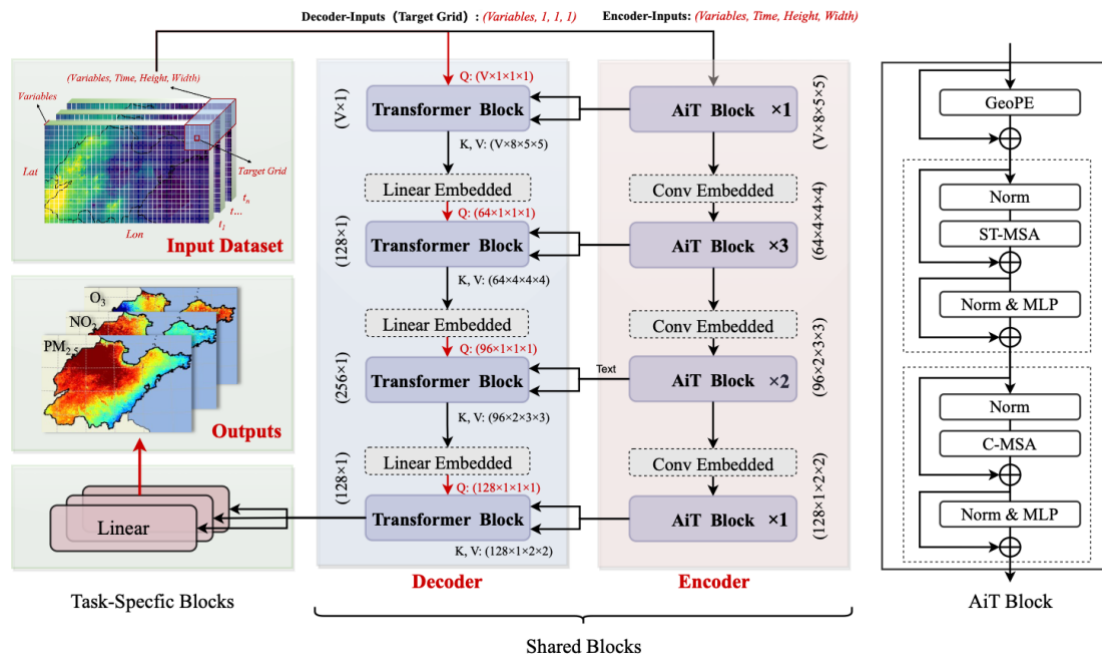
201

202 **Figure 1.** Schematic diagram of the AiT model. The white box of multi-dimension
203 inputs presents each pixel of raster data. The AiT Block is a Transformer block based
204 on self-attention across space, time, and variables. The GeoPE, Norm, MLP, ST-MSA
205 and C-MSA indicate respectively positional embedding, layer normalization, multi-
206 layer perceptron, spatial-temporal multi-head self-attention and multi-channels (multi-
207 variables) multi-head self-attention.

2.3 Diagnosing O_3 Formation Sensitivity

208

209   Interpretability can provide insight into how a model may be improved, bolster the

210   understanding of the process being modeled, and engender appropriate confidence

211   among researchers. SHAP is a coalitional game-theoretic approach based on Shapley

212   values (Shapley, 1988) and then assigns each variable an importance value for a

213   particular estimation. Deep SHAP, a high-speed approximation algorithm that builds on

214   the connection between Shapely values and DeepLIFT (Shrikumar et al., 2019), is

215   employed to compute the feature importance of AiT from all data with monitoring

216   labels for interpreting the prediction. The sensitivity of the O_3 formation regime was

217   deduced using a combination of the XGBoost model and SHAP interpretability method,

218   employing the GPUTreeShap algorithm (Mitchell et al., 2020), which simulated the

219   response of surface O_3 to meteorological conditions, HCHO, NO_2 and $PM_{2.5}$, by

220   utilizing the continuous estimations from ERA5, AiT and TROPOMI between 2019 and

221   2020. The incorporation of meteorology in the model ameliorated the inadequacies in

222   the conventional method (HCHO-NO_2 ratio), where its thresholds for identifying O_3

223   regimes vary temporally and spatially. The positive or negative contributions of three

224   atmospheric pollutants were used to identify their promoting or inhibitory effects on O_3

225   variability. Given the unbiased property of SHAP values regarding directionality, the

226   normalized relative magnitudes of SHAP values were calculated for HCHO, NO_2, and

227    $PM_{2.5}$. This allowed the differentiation of the O_3 formation regimes based on the locally

228   maximal proportions of the SHAP values for each species. The ground-level monthly

229   HCHO concentrations were derived using a combination of column-to-surface

230   conversion factor (CF) simulated from the ECMWF Atmospheric Composition

231   Reanalysis 4 and the tropospheric HCHO VCDs obtained from TROPOMI (Cooper et

232   al., 2022; Su et al., 2022; Inness et al., 2019). A detailed description of the CF method

233   as used here is discussed in Text S7. To ensure consistency in resolution between

234   TROPOMI and AiT, we employed the oversampling method to downscale the

235   TROPOMI VCDs to the resolution of AiT estimation, which has been proven effective

236   in achieving finer resolution (Su et al., 2022; Cooper et al., 2022; van Donkelaar et al.,

237   2015).

238   **3. RESULTS AND DISCUSSION**

239   **3.1 Performance Evaluation for the AiT**

240   **3.1.1 Cross-validation Metrics**

241   We evaluated the AiT performance using the 10-fold CV approach (Text S8), with

242   correlation coefficient (R^2) measuring the extent to which model simulations explain

243   variability in atmospheric pollutants, and root mean square errors (RMSE) and mean

244   absolute errors (MAE) evaluating the bias/error of the estimates. As shown in Fig. 2,

245   out-of-sample CV daily ground-level O_3, NO_2, and $PM_{2.5}$ estimations are highly

246   consistent with ground observations ($R^2 = 0.96, 0.92, 0.95$), indicating low uncertainties,

247   with RMSE of 10.1, 4.7, and 8.5 $\mu g/m^3$ and MAE of 7.2, 3.5, and 5.3 $\mu g/m^3$ for the

248   2018-2021 period. The linear regression comparing the O_3 predictions versus

249   observations yields a slope of 0.98 and an intercept of 2.39, which demonstrates that

250 there is no systematic bias in the estimations. Meanwhile, as shown in Fig. S3, our AiT

251 model performs well at the individual-site scale with high CV-RMSE for O_3, NO_2, and

252 $PM_{2.5}$ (10.5 ± 8.6, 4.7 ± 1.1, and 8.3 ± 2.8 µg/m³). In general, the AiT model is robust

253 for multi-pollutant simultaneous estimations.
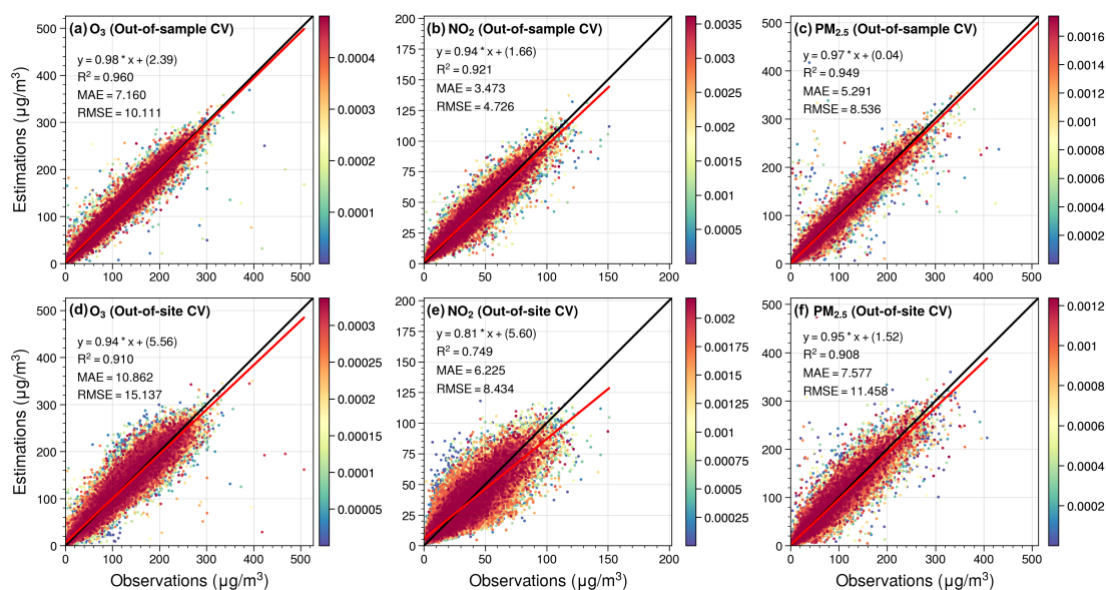
255 **Figure 2.** Out-of-sample cross-validation (a-c) and out-of-site cross-validation (d-f) of

256 daily ground-level O_3, NO_2 and $PM_{2.5}$ concentration in the validation set.

257 The spatial generalization ability of the AiT is then examined by the out-of-site CV

258 evaluation method (Fig. 2). The daily spatial variations of O_3, NO_2, and $PM_{2.5}$ at

259 locations without ground measurements can be well estimated by our model (i.e., CV-

260 R^2 = 0.91, 0.75, 0.91), representing a core contribution of such studies. We also probe

261 the model performance for each site separately based on spatial CV estimations (Fig.

262 S4). This general model yields an RMSE of 15.2 ± 8.8, 8.1 ± 2.7, and 11.1 ± 2.8 µg/m³,

263 respectively. Furthermore, we trained the AiT model using data exclusively from

264 CNEMC and assessed its generalizability by validating it with data from SDEM. The

265 model demonstrates strong performance with high our-of-sample CV R^2 values in the

266 validation dataset of CNEMC (Fig. S5), and when evaluated with SDEM data, it

267 exhibits only an acceptable degradation in predictive accuracy (Fig. S6, R^2 for O_3, NO_2,

268 and $PM_{2.5}$: 0.90, 0.73, 0.79). Meanwhile, our framework utilizes multi-task learning to

269 enhance computational efficiency through a single iteration and leverages the

270 interactions among multiple pollutants to optimize the performance at individual

271 pollutant levels (Table S2). In summary, AiT provides relatively stable estimations in

272 areas without available ground-level monitoring and reliably extends ground

273 monitoring from the site scale to the full-coverage spatial scale with high spatial

274 resolution.

275 **3.1.2 Compared with Other ML Models**

276 Since ground-level air quality measurements across the target regions are

277 extremely limited at a 500 m spatial resolution, representing only roughly two-

278 thousandths of the total grid cells, we seek implicit approaches to validate our estimated

279 near surface pollutant concentrations. We compared the model performance with

280 previous studies that applied different ML methods to estimate these three air pollutants

281 individually and found out that our cross-validation results are comparable or even

282 better than those (Table S3). We also created a new dataset in our study by applying the

283 classic RF algorithm which is the most common ML model for estimating atmospheric

284 pollution in recent years (Wei et al., 2022a; Requia et al., 2020; Xiao et al., 2018; Geng

285 et al., 2021; Lu et al., 2021) with the same variables as AiT. The statistical comparisons

286   between AiT and RF are also shown in Table S3. We then compared the spatial

287   distribution of our results with estimations from CHAP, AiT-CNEMC, and RF.

288   Figure 3 shows the spatial maps of near-surface air pollutants with partially

289   zoomed satellite images for monitoring sites, AiT, CNEMC-trained AiT, RF, and CHAP

290   in 2019 (see Fig. S7 for 2020). We found that the estimated NO_2 and $PM_{2.5}$ from the

291   AiT share a similar spatial distribution to those estimated by RF and CHAP. However,

292   enlarged city-level urban regions in Fig. 3 reveal that AiT estimates fine structures and

293   intra-urban disparities in near-surface multi-pollutant concentrations, which cannot be

294   captured by either RF or CHAP products. This spatial gradient is also captured by AiT

295   trained with CNEMC data, revealing the reliability of the deep learning model structure.

296   In general, while RF and CHAP can only identify the hotspots of air pollutants at a

297   regional scale, the spatial distribution of air pollutants estimated by AiT shows much

298   more detailed differences with high spatial and temporal variability across the city scale.

299   The differences of near-surface annual averaged pollutants between 2019 and 2020 for

300   measured and multi-estimated data are presented in Fig. S8. The reductions or increases

301   of O_3, NO_2, and $PM_{2.5}$ in distinct locations can be simulated by our model, which is

302   relatively consistent with the changes of measurements. The zoomed maps in Fig. S8

303   show the differences in three pollutant concentrations at the city scale of the capital of

304   Shandong Province, Jinan. It can be found that the change in pollutant levels in 2020

305   compared to 2019 exhibits substantial regional variations and intra-urban heterogeneity,

306   with some areas experiencing an increase while others a decrease. Compared to the

307 estimations of RF and CHAP, our results successfully capture the complex distribution

308 of air pollution in reality and reveal that the decline in PM$_{2.5}$ is primarily concentrated

309 in suburban areas, while an increase is pronounced in some regions of urban during

310 2020. Notably, this spatial trend may be consistent with underlying emission patterns

311 and meteorological conditions.
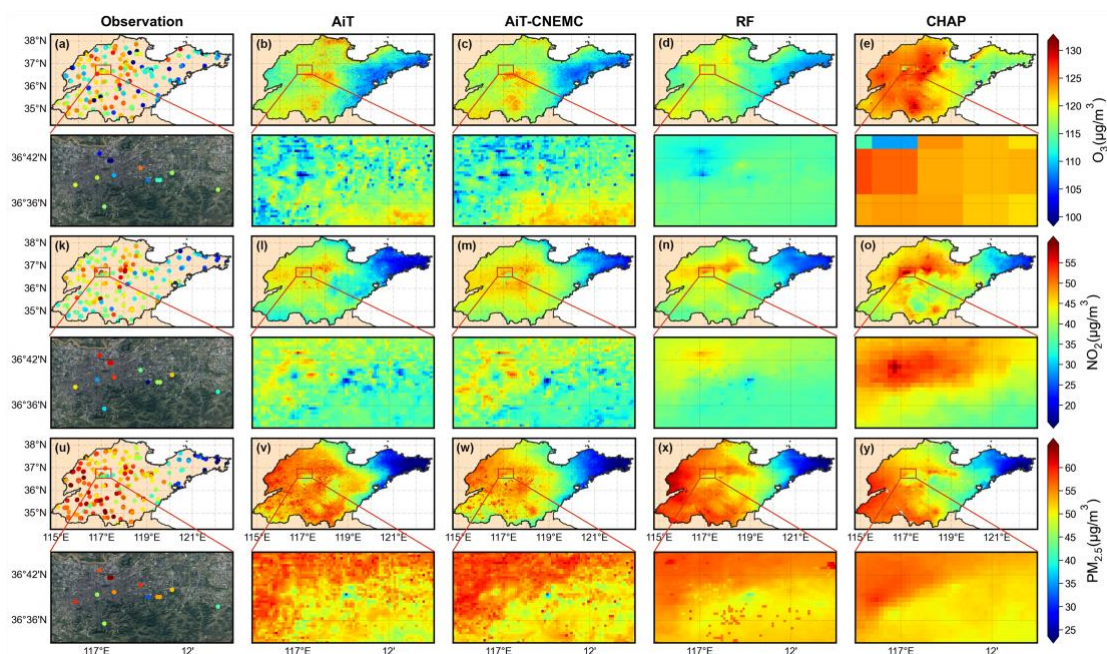
313 **Figure 3.** Spatial distribution of the annual mean (a-e) O$_3$, (k-o) NO$_2$, and (u-y) PM$_{2.5}$

314 concentrations from observations, Air Transformer (AiT), CNEMC-trained AiT,

315 Random Forest (RF) and ChinaHighAirPollutants (CHAP), respectively, in 2019. The

316 region enclosed by the red rectangular box corresponds to the zoomed-in maps of the

317 satellite (© Tianditu: www.tianditu.gov.cn) and pollutant concentrations at a city scale

318 for the capital city of Shandong Province, Jinan.

319 **3.1.3 Typical Event Study**

320 The typical example of the spatial distribution of multi-pollutant observations and

321 estimations of AiT is compared for validating the predictive capability of the model at

322 a particular pollution episode, i.e., 13-16 March 2021. During this period, an early

323 season dust storm, which was called the largest and strongest such storm in a decade,

324 hits northern China (Myers, 2021). As shown in Fig. 4, our model can capture the spatial

325 distribution of surface O_3, NO_2, and $PM_{2.5}$ in the time of severe atmospheric pollution.

326 In addition, our estimations are in high concordance with measurements in terms of

327 magnitudes and spatial variability over the entire research region. The model trained

328 solely on CNEMC data is also capable of effectively capturing the drastic changes in

329 air quality during the pollution episode (Fig. S9). Combining wind fields to analyze

330 $PM_{2.5}$ distribution on the day of the dust storm, it can be found that surface wind carries

331 a massive amount of particulate matter from Beijing, which suffered a severe dust storm,

332 to northern Shandong. The influence was gradually diminishing in southern Shandong

333 due to the obstruction of Mount Tai. Spatial heterogeneity within intra-urban areas was

334 further investigated to identify the hotspots of pollution sources. The satellite images in

335 even-numbered rows of Fig. 4 illustrate the spatial disparities of three pollutants around

336 four typical emission sources: thermal power plants, industrial parks, overpasses, and

337 parks. As depicted, these anthropogenic emission sources contribute to higher pollution

338 levels, while the mountain in the park mitigates primary pollution but also increases O_3

339 concentrations. Industrial sources emit a large number of NO_x and $PM_{2.5}$, leading to

340 increased pollution of these species compared with other urban microenvironments,

341 which in turn promotes O_3 formation, particularly in downwind areas (Miller et al.,

342 1978; Tang et al., 2020). Although the spatial gradients of pollutants on the street are

343 not as apparent as in the dataset with 100 m resolution (Huang et al., 2021), the

344 predicted spatial variation between various geographical scenes is in satisfactory

345 agreement given the 500 m scale of the model. Urban areas affected by diverse dust

346 pollution exhibit lower $PM_{2.5}$ concentrations compared to rural due to the obstructive

347 and filtering effects of artificial structures, such as buildings and urban greenery (Fig.

348 S10), which cannot be effectively captured solely by ground-based observations.

349 Notably, the elevated $PM_{2.5}$ inhibits the formation of O_3 by diminishing solar radiation

350 flux and absorbing the HO_2 radical on the aerosol surface, even in conditions

351 characterized by similar NO_2 levels. As for the mapping, AiT accurately grasps the

352 spatial characteristics of air pollutants and delivers a coherent spatial-temporal

353 distribution that is consistent with the prior knowledge of atmospheric transport.
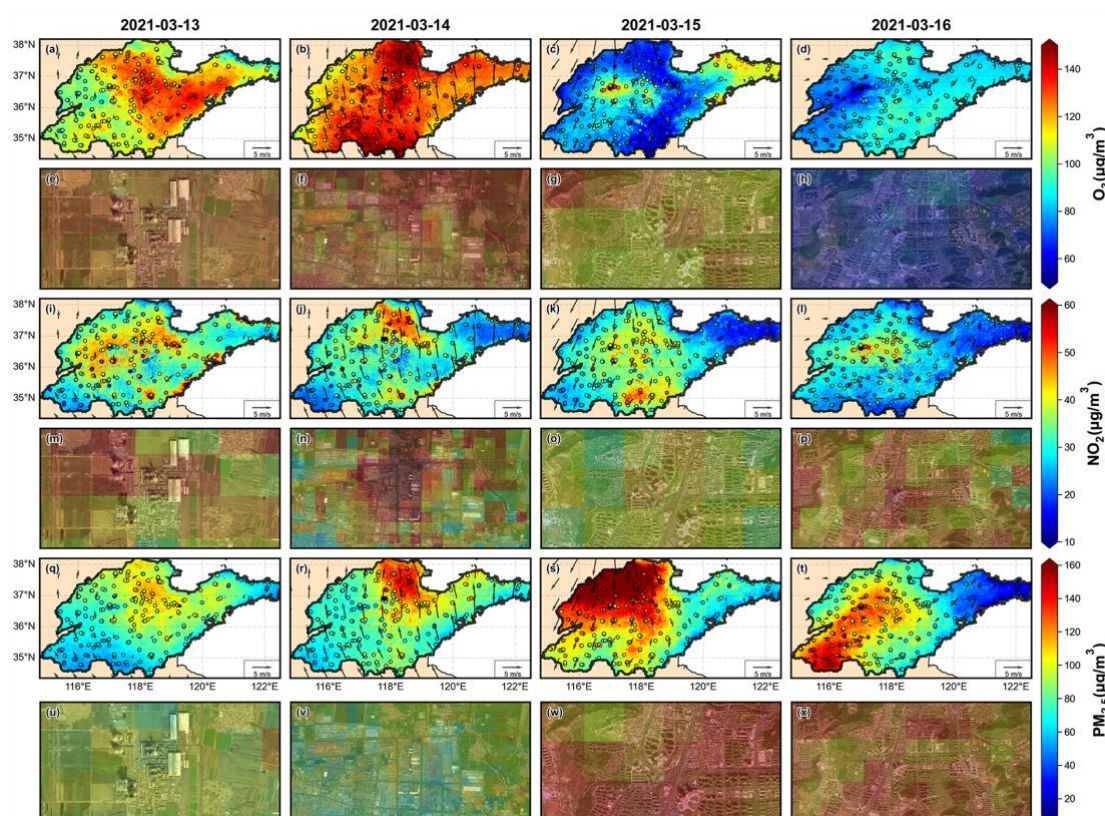
354

355 **Figure 4.** The spatial distribution of ground-level O_3 (a-d), NO_2 (i-l), and $PM_{2.5}$ (q-t)
356 concentrations from AiT and monitoring stations during 13-16 March 2021 in

Shandong, China. The black arrows are the 10 m wind speed and wind direction. The even-numbered rows correspond to the concentration distribution maps of typical emission sources for the respective pollutants, accompanied by satellite images (© Tianditu: www.tianditu.gov.cn). The upper right area of e, m, and u is a thermal power plant in Weifang City (119°250′ E-119°280′ E, 36°658′ N-36°673′ N). The center area of f, n, and v is an industrial park in Zibo city (117°725′ E-117°845′ E, 36°880′ N-36°940′ N). The center and upper right area of g, o, and w is an overpass and Wanling mountain in Jinan city (116°977′ E-117°009′ E, 36°590′ N-36°606′ N). The center area of h, p, and x is another overpass in Jinan city (116°970′ E-117°030′ E, 36°580′ N-36°610′ N).

3.2 Urban-nonurban Difference

Full-coverage pollutant estimates provide a foundational basis for assessing urban-nonurban disparities, addressing the critical issue of imbalanced site numbers between urban and rural locations. Table S4 shows the concentrations of O_3, NO_2, $PM_{2.5}$, and HCHO over the urban and nonurban regions, delineated from an annual urban extent dataset (Zhao et al., 2022). The urban extents in Shandong Province in 2019 are depicted in Fig. S11. From 2019 to 2020, surface air pollutant levels declined significantly in Shandong. The averaged concentration discrepancies of these pollutants between urban and nonurban over February to March (lockdown during COVID-19) and June to October (summertime) are shown in Fig. 5. Surface concentrations of NO_2 and HCHO are higher in urban than nonurban areas, and the differences narrowed from February to October, while $PM_{2.5}$ is the opposite at both. Ground-level O_3 levels exhibited unexpected urban-nonurban disparity variations, from the lockdown period through the summer, as well as from 2019 to 2020. Compared to nonurban areas, the urban areas, which previously had lower O_3 levels, began to experience higher

382 concentrations, attributed to a more rapid decline of ozone in nonurban regions. Figure

383 6 revealed that urban-nonurban differences in O_3 and $PM_{2.5}$ varied across various cities

384 during the lockdown period in 2019, while the higher NO_2 pollution in urban areas

385 remained consistent. In summer, only a handful of urban areas exhibit lower levels of

386 ozone concentration, where NO_2 and $PM_{2.5}$ levels surpass those in nonurban regions,

387 attributable to a more pronounced titration effect of NO and a slower rate of

388 photochemistry reactions (Fig. S12) (Sicard et al., 2016, 2020; Zhang et al., 2004).

389 Comparative urban-nonurban differences from 2019 to 2020 indicate an accelerated

390 reduction of ozone and HCHO in non-urban areas, while NO_2 and $PM_{2.5}$ levels in urban

391 have seen a more significant decrease due to the decline in anthropogenic activities,

392 particularly the suspension of emissions from pollution sources located in urban areas.

393 Upon comparing the results of urban-nonurban disparities of our data with monitoring

394 data and the CHAP dataset, we have identified potential overestimations or

395 underestimations across various cities in monitoring data, likely resulting from the

396 limited number of non-urban sites (Figs. 6p and S13). The notable disparity between

397 the number of urban and non-urban sites in cities such as JNA, LC, LY, QD, and YT

398 results in a pattern of urban-nonurban differences that contrasts markedly with the

399 observed in AiT (Table S5). The urban-nonurban difference calculated by the CHAP

400 generally aligns with our findings (Fig. S14). Nevertheless, it is worth noting that the

401 coarse resolution of O_3 (10 km) has led to a significant overestimation. These results

402 highlight the invaluable of high-resolution and gapless data for studying urban-

403   nonurban disparities.
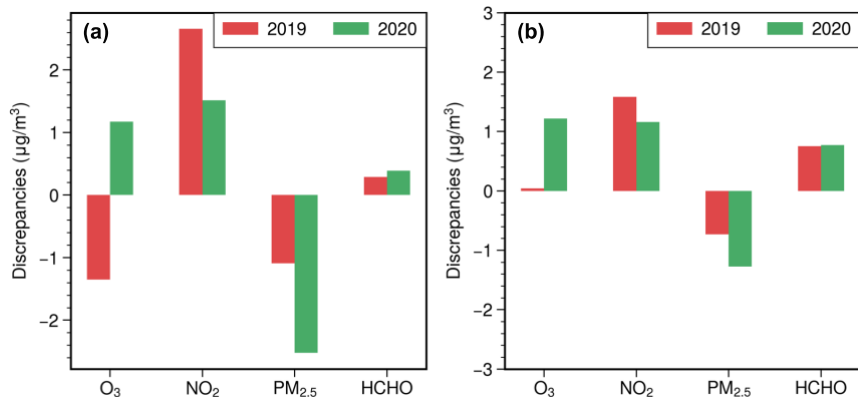
404

405   **Figure 5.** The discrepancies of O_3, NO_2, and $PM_{2.5}$ between urban and non-urban from

406   2019 to 2020 for the lockdown period (a) and summertime (b) averaged concentration.
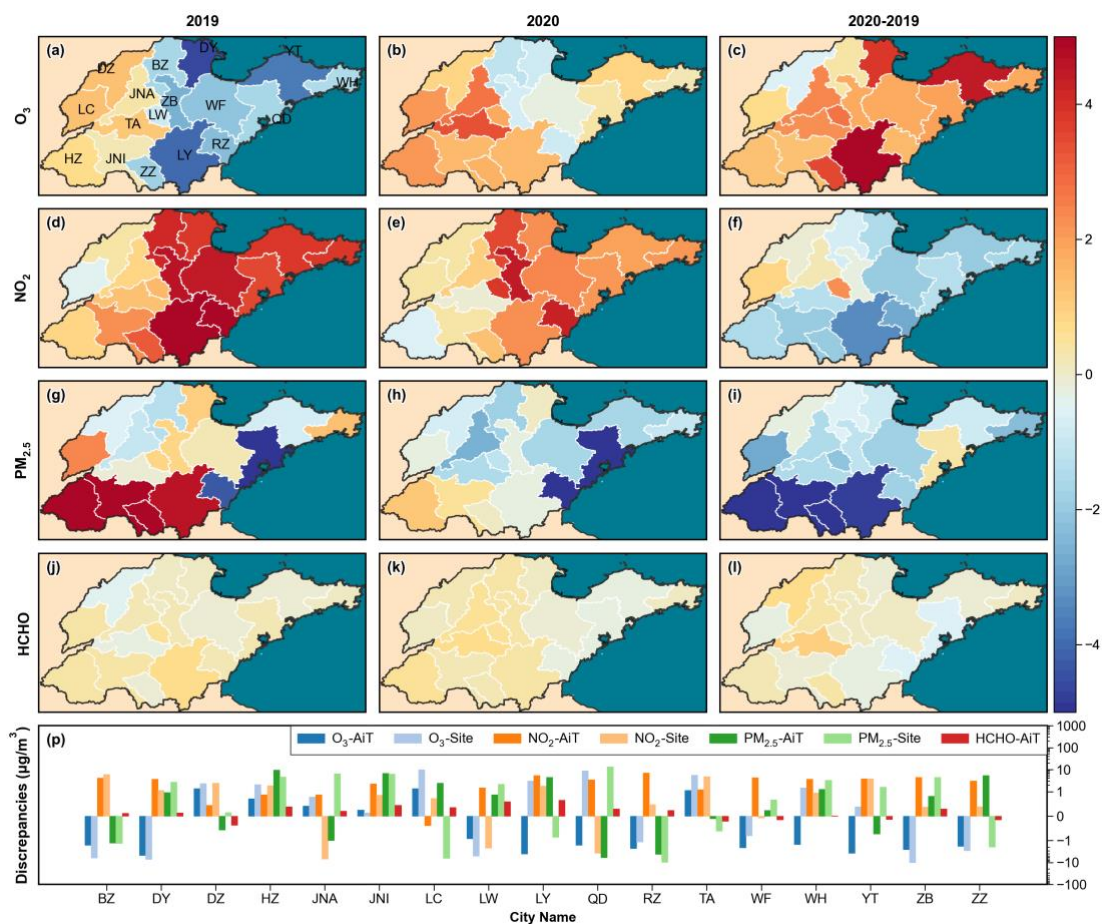
407

408   **Figure 6.** The urban-nonurban disparities of O_3, NO_2, $PM_{2.5}$, and HCHO calculated by

409   AiT across cities with administrative divisions in Shandong, China during lockdown

410   periods in 2019 (a, d, g, j) and 2020 (b, e, h, k), and the changes of differences between

411   2019 and 2020 (c, f, i, l). P is the comparison between the results of monitoring station

412   data and the AiT dataset in 2019. The red color represents a greater decline in air

pollutants in nonurban areas, while the blue color indicates a more significant reduction in urban areas in the third column of the figure. (YT: Yantai, BZ: Binzhou, DY: Dongying, WH: Weihai, DZ: Dezhou, JNA: Jinan, QD: Qingdao, WF: Weifang, ZB: Zibo, LC: Liaocheng, LW: Laiwu, TA: Taian, LY: Linyi, RZ: Rizhao, JNI: Jining, HZ: Hezhe, ZZ: Zaozhuang)

3.3 Photochemical Regimes

3.3.1 Ozone-NO_x-VOCs-Aerosols Sensitivity

Figure S15 shows the seasonal maps of O_3, $PM_{2.5}$, and NO_2 estimations from AiT, and satellite-derived surface HCHO. Based on these data, we first capture the well-established non-linearities in O_3-VOC-NO_x chemistry by a conceptual framework similar to classic O_3 isopleths typically generated with models (Pusede et al., 2015; Ren et al., 2022a). Figure 7a depicts O_3 concentration as a function of HCHO and NO_2, which was derived solely from ground-level estimation. The result indicates that the O_3 regimes can be qualitatively identified based on the nonlinear interaction between surface O_3, HCHO, and NO_2. In the regime characterized by high NO_2 and low HCHO, the elevated consumption of HO_x, predominantly driven by the $OH + NO_2$ termination reaction, results in the suppression of NO_x on O_3, indicating the prevalence of VOC-limited chemistry. Conversely, when HCHO levels are high and NO_2 levels are relatively low, O_3 increases with NO_2 and exhibits insensitivity to HCHO due to abundant peroxyl radicals (HO_2 + organic peroxy (RO_2) radicals, RO_x) self-reactions, suggesting NO_x-limited (VOC-saturated) chemistry. In cases where high HCHO and NO_2, the O_3 increases with both HCHO and NO_2, reaching a peak. While Fig. 7a resembles this overall O_3-VOC-NO_x, the blurry transition between two different

436 regimes and the role of $PM_{2.5}$ is uncertain which may be influenced by meteorological

437 conditions, chemical and depositional loss of O_3, errors of estimations, and "aerosol-

438 inhibited". Increasing $PM_{2.5}$ levels could suppress O_3 formation even under high HCHO

439 and NO_2 conditions (Fig. 7b), which could be induced by enhanced reactive uptake of

440 HO_2 onto aerosol particles and weaker photochemical reaction resulting from the

441 scattering and absorption of solar radiation by anthropogenic aerosols. The relationship

442 between $PM_{2.5}$ and O_3 in Shandong demonstrates the distinct stages of O_3 chemistry, as

443 depicted in Fig. 7c. When $PM_{2.5}$ was below the maximum turning point (MTP1, 35

444 $\mu g/m^3$), a linear and positive correlation between O_3 and $PM_{2.5}$ was observed due to the

445 common dependence on precursors in the initial stage (Zhang et al., 2022). As $PM_{2.5}$

446 increased beyond the MTP1, a sharp reduction in HCHO and O_3 was observed,

447 accompanied by a decline in surface short-wave radiation, reflecting their formation as

448 photo-oxidation products of OVOCs and NO_x. When $PM_{2.5}$ exceeded the minimum

449 transition point (MTP2, 45 $\mu g/m^3$), a phase was observed with stagnant radiation

450 intensity and relatively higher NO_2 levels compared to HCHO. This regime is typically

451 associated with a VOC-limited regime, where an increase in HCHO and a decrease in

452 NO_2 concentration could promote O_3 production. However, our findings demonstrated

453 an opposite impact of HCHO and NO_2 on O_3 when $PM_{2.5}$ exceeded MTP2. Figure **7**d

454 shows the changes in the quantitative relationships between HCHO/NO_2 (FNR) and O_3

455 by artificially changing $PM_{2.5}$ and precursors levels for XGBoost, in which the peak of

456 curves marks the transitional threshold of O_3 regimes from VOC to NO_x sensitive. It

457 can be seen that attenuated $PM_{2.5}$ pollution could increase the sensitivity of O_3 to VOCs

458 and decrease the sensitivity to NO_x, which causes the shift in O_3 regimes from NO_x-

459 limited to VOC-limited. With the recent reduction in NO_x emissions in China, the

460 anticipated transition of the O_3 production regime in urban areas towards being more

461 NO_x-limited has been impeded by the heightened VOC sensitivity resulting from

462 decreased $PM_{2.5}$ levels. Our results are consistent with the findings of Li et al. regrading

463 O_x-NO_x relationship in response to changing $PM_{2.5}$ (Li et al., 2022a), and with the

464 findings of Dyson et al. on the impact of HO_2 aerosol uptake on O_3 production (Dyson

465 et al., 2023). The SHAP interaction plots in Fig. 7e and f illustrate that the influence of

466 NO_2 and HCHO on O_3 formation is not constant and is influenced by the levels of $PM_{2.5}$.

467 Typically, at a certain level of $PM_{2.5}$, a lower NO concentration results in a stronger

468 inhibitory effect on O_3 production. This could be due to aerosols exerting stronger

469 suppression through the HO_2 sink at lower NO_x levels. As the concentration of $PM_{2.5}$

470 increases, often accompanied by a concurrent increase in NO_2 as a key precursor, there

471 is a greater need for higher levels of NO_2 to be converted into nitrous acid (HONO)

472 through the heterogeneous uptake by aerosols. This process produces more OH radicals,

473 which facilitate photochemical O_3 formation, thereby offsetting the increased inhibitory

474 effect of the HO_2 sink. Under high $PM_{2.5}$ concentrations, an increase in NO_2 along with

475 a decrease in HCHO enhances their effect on promoting O_3 formation. This

476 enhancement could be caused by increased titration of O_3 by NO, resulting from weaker

477 conversion of NO to NO_x through the RO_x radical. Meanwhile, the impact of HCHO

478   shifts from promoting to suppressing as PM$_{2.5}$ pollution intensifies. It further illustrates

479   that the scavenging of HO$_2$ on aerosols can cause the shift in O$_3$ regimes from being

480   VOC-limited to NO$_x$-limited and the threshold approach is restricted by aerosols and

481   meteorology for determining the constantly changing O$_3$ formation regimes over time

482   and space.
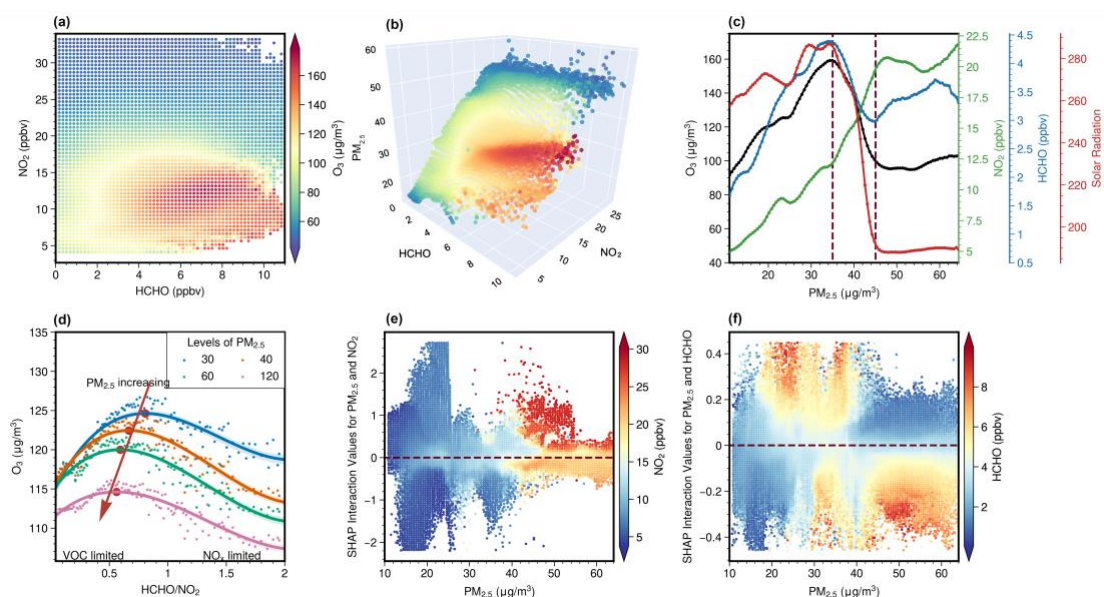
483

484   **Figure 7.** (a) O$_3$ concentrations as a function of surface HCHO and NO$_2$. (b) O$_3$

485   concentrations as a function of surface HCHO, NO$_2$, and PM$_{2.5}$. Both A and B utilize a

486   shared color bar to indicate O$_3$ concentrations, enhancing comparability. (c)

487   Relationship between O$_3$, and NO$_2$, HCHO, and surface short-wave radiation flux. The

488   paired O$_3$, HCHO, NO$_2$, and solar radiation are divided into 100 bins based on PM$_{2.5}$

489   and then the averaged concentrations (y-axis) are calculated for each PM$_{2.5}$ bin (x-axis).

490   (d) Changes in HCHO/NO$_2$-O$_3$ relationship in response to changing PM$_{2.5}$ by XGBoost

491   model. The solid lines are fitted with four-order polynomial curves, and the shading

492   indicates 95% confidence intervals. (e-f) The interaction SHAP values reveal an

493   interesting hidden relationship between pairwise variables (PM$_{2.5}$ and NO$_2$, HCHO) and

494   O$_3$.

495   Unraveling the intricate interplay of O$_3$ with meteorology, aerosols, and precursors

496   that govern O$_3$ formation over extensive spatial domains has long confounded robust

497   interpretation. These multiscale processes were elucidated using an interpretable ML

498   model, which can quantify the positive or negative contributions of individual processes.

499   As depicted in Fig. S16, the performance of the XGBoost model is robust, evidenced

500   by a high R^2 value of 0.99 coupled with a low RMSE of 3.24 $\mu g/m^3$ and MAE of 2.33

501    $\mu g/m^3$. Figure S17 elucidates that meteorological variations, chiefly surface short-wave

502   radiation flux modulating photochemical reaction kinetics, primarily dictate the

503   heterogeneous geographic distribution of O_3 at the regional scale, with lower levels

504   over the Jiaodong Peninsula. Meanwhile, local atmospheric chemical processes

505   predominate the city-scale variability of O_3. HCHO facilitated O_3 formation in urban

506   areas yet suppressed it in rural regions across areas with high ozone, where most NO_2

507   promoted O_3 production overall, indicating VOC-NO_x synergistic control on O_3 in cities

508   and a NO_x-limited regime in rural areas during summertime. The contribution of NO_2

509   and $PM_{2.5}$ exhibits analogous seasonal variability, promoting O_3 formation under low

510   pollution conditions while inhibiting O_3 when pollution levels are high (Figs. S15 and

511   18). The elevated NO_2 levels in autumn led to a negative contribution to O_3, whereas

512   the facilitating effect of $PM_{2.5}$ was enhanced. This stems from the relatively moderate

513    $PM_{2.5}$ concentrations slightly affecting photochemical reaction rates, while the

514   increased NO_2 amplified the reactive uptake of NO_2 by $PM_{2.5}$, generating more OH

515   radicals that promote O_3 formation (Lin et al., 2023; Tan et al., 2022). In winter, $PM_{2.5}$

516   pollution exceeding 75 $\mu g/m^3$ suppressed O_3 formation through scattering and

517   absorbing solar radiation that activates atmospheric chemical processes, which

518   counteracted the promoting effect of high $PM_{2.5}$ through the conversion of NO_2 to

519   HONO.
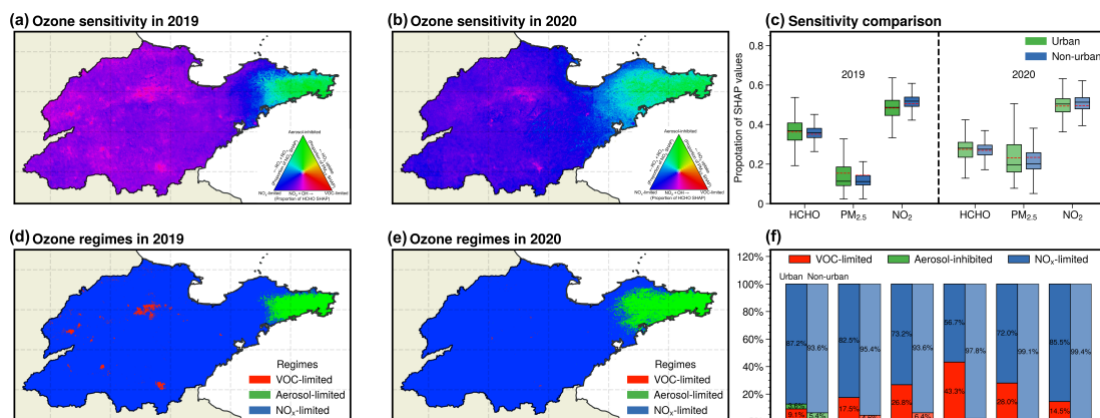
521   **Figure 8.** Comparison of geographical distribution for ozone formation regimes
522   between 2019 and 2020 in the summertime. All surface daily O_3, $PM_{2.5}$, and NO_2
523   estimations from Air Transformer (AiT) are averaged over each month from May to
524   October 2019-2020 for matching monthly HCHO derived from TROPOMI (500 * 500
525   m). (a, b) Geographical distribution of fractional contribution of chemical factors
526   representing O_3 formation regimes. The ternary phase diagram in the legend depicts the
527   normalized fraction of SHAP values for O_3 attributed to HCHO, NO_2, and $PM_{2.5}$ at the
528   surface, representing VOC-limited (red), aerosol-inhibited (green), and NO_x-limited
529   (blue) regimes, respectively. (c) Statistical Changes in the fractional contribution of
530   chemical factors. (d, e) Geographical distribution of O_3 chemical regimes. (f)
531   Proportion of three O_3 chemical regimes across urban and nonurban areas in 2019 in
532   Shandong (SD), and individual cities (BZ: Binzhou, ZB: Zibo, LC: Liaocheng, LY:
533   Linyi, JNI: Jining).

534   Figure 8a-c shows surface distribution and changes of the relative proportions of

535   SHAP values on three pollutants for inferring O_3 photochemical regimes. Moving along

536   an urban-to-rural gradient, reactions dominated by RO_x radical self-reactions are

537   continuously enhanced with increasing NO_x SHAP values, resulting in the majority of

538   rural Shandong being situated in NO_x-limited regimes. Furthermore, the overall ozone

539   production regimes in Shandong exhibited a transition toward more NO_x-limited from

540   2019 to 2020, with regions dominated by NO_x-limited shifting toward being aerosol-

inhibited in the Jiaodong Peninsula. The aerosol-inhibited regime differs from either of

the two classically applied tropospheric O_3 policy-control regimes. It is attributed to the

predominant heterogeneous HO_2 uptake by aqueous aerosols, despite comparatively

low $PM_{2.5}$ levels during summertime. The marine environment engenders liquid aerosol

particles with HO_2 uptake coefficients exceeding those of dry aerosols by orders of

magnitude (Song et al., 2022a). Concurrently, lower ambient NO_x levels minimize the

promotive effects of aerosols on ozone formation (Tan et al., 2022; Kohno et al., 2022).

This result is consistent with the findings of Dyson et al. (Dyson et al., 2023), which

concluded that the contribution of HO_2 sinks onto aerosols on total HO_2 could increase

for areas with low NO levels. The attenuated responsiveness of O_3 formation to VOCs

induced by the uptake of HO_2 results in enhanced sensitivity of NO_x at the northwest

boundary region of the Jiaodong Peninsula. Collectively, these processes delineate an

aerosol-inhibited ozone production regime in this coastal region, reflecting the

sensitivity of O_3 photochemistry to the HO_2 sink. In several cities, including Binzhou,

Zibo, Liaocheng, Linyi, and Jining, a greater proportion of urban areas, as compared to

their nonurban counterparts, exhibited a VOC-limited regime in 2019, as indicated by

the prevalence of red regions in Fig. 8d. The percentage of urban areas in these cities

under a VOC-limited regime ranges from 15% to 43%, in stark contrast to non-urban

areas where such a regime is typically rare (Fig. 8f). The comparison of O_3 sensitivities

from 2019 to 2020 shows a regional shift towards increased sensitivity to aerosol and

NO_x, along with a decreased VOC sensitivity as a result of NO_x reduction (Fig. 8a-c).

562   This shift has led to the majority of areas in Shandong being dominated by a NO$_x$-

563   limited regime in 2020, with an expanded aerosol-inhibited regime region in the

564   Jiaodong Peninsula (Fig. 8e). Additionally, the discrepancy in O$_3$ formation sensitivity

565   between urban and non-urban areas has been diminishing during this period (Fig. 8c).

566   As illustrated in Fig. 9, while the ozone regime transitions towards NO$_x$-limited, there

567   is a marked shift towards greater aerosol sensitivity across nearly 90% of areas, leading

568   to a 1.6% increase in aerosol-inhibited grids. Compared to nonurban regions, a higher

569   number of grids in urban areas demonstrate a shift towards NO$_x$ sensitivity. Conversely,

570   urban areas that were predominantly aerosol-inhibited in 2019 showed a lower

571   sensitivity shift towards NO$_x$.
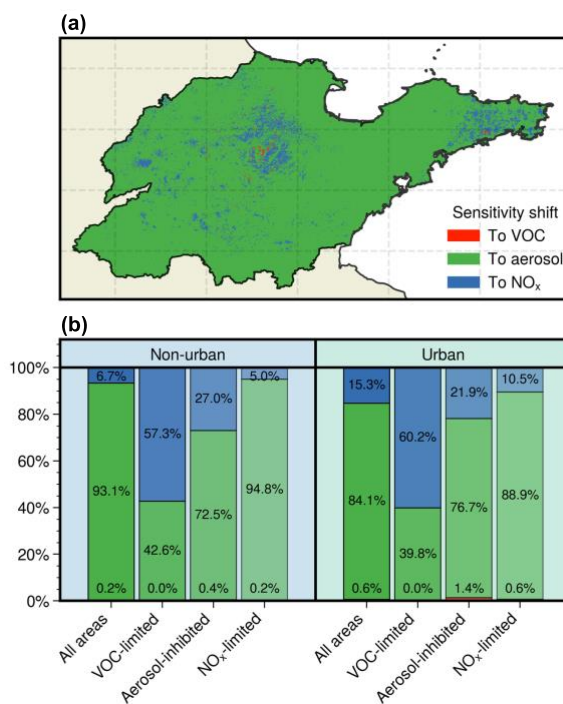
572

573   **Figure 9.** Geographical distribution of changes in ozone sensitivity from 2019 to 2020

574   in summertime (a). Comparison of ozone sensitivity changes across areas dominated

575   by different chemical regimes in 2019 between urban and non-urban areas (b).

3.3.2 Impact on Urban-nonurban Differences

We further explore the reversed O_3 differences by separating the individual contributions of climate and anthropogenic changes using an interpretable machine learning model (Fig. 10). The results demonstrate that atmospheric chemical processes and meteorological conditions commonly dominate the discrepancies in O_3 levels between urban and non-urban areas. From 2019 to 2020, meteorological shifts remained uniform across urban and non-urban regions, marked by lowered surface pressure, boundary layer height, and short-wave radiation, alongside heightened precipitation. This, coupled with decreased precursor levels, contributed to a decline in O_3 pollution. As shown in Fig. 10 and S19, the diminished reduction in boundary layer height and radiation flux across urban areas, compared to nonurban areas in 2020, decelerated the expected decline of O_3 concentrations, leading to urban O_3 levels exceeding those of nonurban areas. Concurrently, a narrowing difference in temperatures between urban and nonurban areas, despite an overall cooling from 2019 to 2020, favored O_3 formation in urban regions during the summertime. Additionally, $PM_{2.5}$ emerged as the principal anthropogenic factor inverting the urban-nonurban O_3 disparity over the course of 2019 to 2020. Its contribution to ozone shifted from being lower in urban areas to exceeding that in nonurban areas, revealing that the decreased reactive uptake of HO_2 from aerosols induced by a more substantial reduction in $PM_{2.5}$ in urban areas made the larger contribution to O_3 production (Ivatt et al., 2022; Li et al., 2017). Moreover, the response of O_3 to the changes in its precursors and $PM_{2.5}$ was determined by the O_3 formation

597 regimes. The variations in O₃ sensitivity also corroborate the above finding. In rural

598 areas, where there was a lesser reduction in PM$_{2.5}$ concentration, the sensitivity

599 increasingly favored aerosol suppression across more than 93% of the assessed grids

600 (Fig. 9). This enhanced suppression effect of aerosols in rural areas leads to a more

601 significant O₃ reduction compared to urban locales. The reduction of NO$_x$ in nonurban

602 areas demonstrated a more effective reduction in O₃ levels, which predominantly

603 shifted towards a NO$_x$-limited regime in 2020. Although urban areas also showed a shift

604 towards being a NO$_x$-limited regime, they exhibited relatively higher sensitivity to

605 VOCs (Fig. 8). The urban areas, characterized by elevated NO$_x$ emissions, exhibited a

606 higher sensitivity to VOCs, and the fraction of aerosol-inhibited areas increased from

607 2019 to 2020, resulting in the control benefits of urban O₃ pollution in 2020 are partially

608 offset by the nonlinear response of O₃ to a greater reduction in NO$_2$ and PM$_{2.5}$, and a

609 smaller decrease in HCHO relative to nonurban areas. Consequently, O₃ exhibits a

610 lower reduction in urban areas as a result of the aforementioned changes.
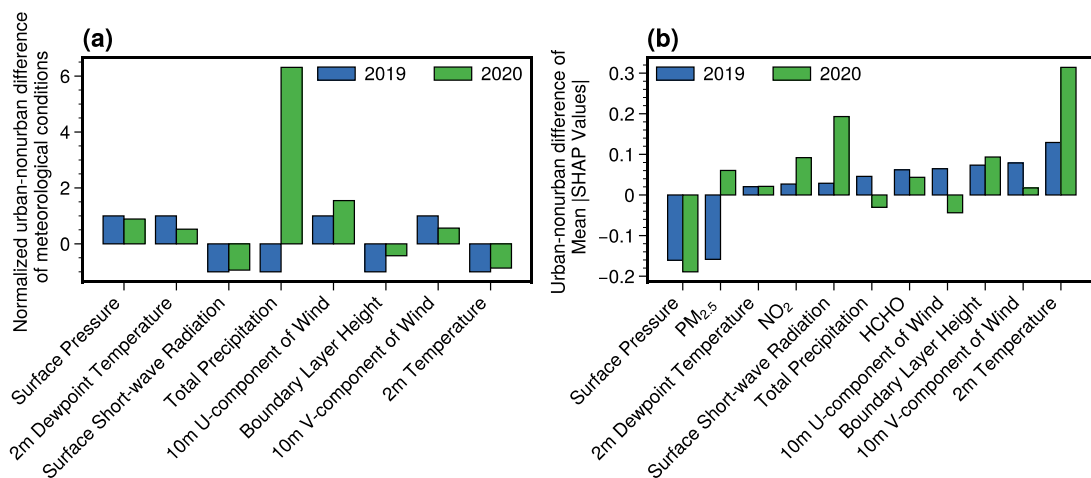
611

612 **Figure 10.** Comparison of urban-nonurban disparities in meteorological conditions (a),

613 and mean absolute SHAP values (b) between 2019 and 2020 across Shandong, China

614 during the summertime.

4. CONCLUSIONS

616   The purpose of the current study was to diagnose the non-linearity of O_3-NO_x-

617 VOCs-aerosols chemistry using an interpretable ML model based on spatially resolved

618 multi-pollutant estimations for determining the causes of changing differences in O_3

619 levels between urban and non-urban areas. Our study represents the first attempt to

620 develop an advanced DL model that reconstructs the concentrations of multiple

621 pollutants and subsequently infers the aerosol-inhibited regime from observations. This

622 innovative approach provides further support for investigating the impact of precursor

623 emissions and aerosol on the urban-nonurban differences in O_3 levels.

624   Given the non-linearity of ozone formation and its increasing regional differences,

625 precise estimations of ground-level O_3, NO_2, HCHO, and $PM_{2.5}$ are crucial for deducing

626 the chemical regimes governing ozone pollution and its urban-nonurban disparities. The

627 evaluation of the model's performance indicates that it can be readily extended to any

628 other domain thanks to its unified architecture. Anyone can easily utilize the model to

629 estimate ground-level pollutants, intelligently considering spatial-temporal

630 neighborhood information based on their customized input data. The model further

631 improved spatial resolution to sub-km levels using TROPOMI and MODIS retrievals

632 via spatiotemporal autocorrelation downscaling of AiT. The "black box" nature of AiT

633 can be made more physically interpretable by SHAP, enabling the evaluation of the

634 significance of each input variable (Fig. S20). The season trends show the highest

635   contribution, followed by emission proxies and meteorological conditions. Meanwhile,

636   the results between AiT trained with all data and that trained exclusively with CNEMC

637   data across various spatiotemporal scales underscore the promising prospect for

638   improving the model's generalization ability with more ground-level monitoring data

639   and the growing space of methods.

640   We conclude that with the effective reduction of $PM_{2.5}$ pollution, the sensitivity of

641   O_3 to VOCs will increase, necessitating further intensification of VOC emissions

642   regulation by government agencies. Three distinct chemical regimes were assessed by

643   tracking NO_x, VOCs, and aerosols with surface NO_2, HCHO, and $PM_{2.5}$. In the

644   Jiaodong Peninsula of Shandong Province, coastal areas with relatively few primary

645   pollutants are widely found to be under an aerosol suppression regime, illustrating that

646   ozone regime inference based on machine learning can serve as an alternative to

647   determining the aerosol suppression regime through the rate of radical termination in

648   atmospheric chemical models. The O_3 regime in other areas of Shandong generally

649   transited from the NO_x-sensitive regime in nonurban to a more VOC-sensitive regime

650   in urban areas. We estimate that substantial reductions in anthropogenic emissions of

651     $PM_{2.5}$ and NO_2 are the main drivers of the reversal of the traditional discrepancy in O_3

652   levels between urban and non-urban areas. In essence, due to the lower efforts in

653   reducing $PM_{2.5}$ in nonurban settings, the aerosol-mediated suppression of ozone

654   became more pronounced, resulting in lower ozone levels in rural areas relative to urban

655   centers. This shift underlines the intricate balance between emission reduction and

656 ozone formation mechanisms, suggesting that nuanced understanding and targeted

657 interventions are necessary to manage and mitigate the health and environmental

658 impacts of such disparities. To preclude exacerbated O_3 pollution resulting from the

659 shift of many regions from VOC-limited to NO_x-limited regimes and the decline in

660 heterogeneous HO_2 uptake induced by $PM_{2.5}$ reduction in urban areas, emission policies

661 aimed at decreasing NO_x to reduce O_3 levels will only be effective with stringent VOC

662 emission abatement when $PM_{2.5}$ is concurrently decreased. The integration of high-

663 resolution pollutant estimations with an interpretable machine learning model offers a

664 promising avenue for advancing our understanding of ozone pollution dynamics and

665 developing effective air quality management strategies.

666 Although our study endeavors to establish O_3 formation regimes involving NO_x,

667 VOCs, and aerosols, and the method identifies an aerosol-inhibited regime from a

668 statistical perspective, it is subject to certain uncertainties due to the relatively poor data

669 quality of HCHO and the unsegregated multiple impacts of aerosols, such as N_2O_5

670 uptake, NO_2 uptake, HO_2 uptake, and light extinction (Tan et al., 2022). We have made

671 efforts to integrate all required surface pollutant concentrations into a unified model,

672 while the absence of ground-level HCHO monitoring data compelled us to tap into an

673 alternative methodology. The retrieval error of surface HCHO and the system error

674 between its retrieval approach and the AiT model degrade the ability of ML to identify

675 the O_3 sensitivity. Meanwhile, the notion of ozone regimes is only appreciated in

676 photochemically active environments where the RO_x-HO_x cycle is active (Souri et al.,

677 2023). The definition of NO_x-limited or VOC-limited regimes is meaningless in

678 nighttime chemistry, where NO-O_3-NO_2 partitioning is the primary driver. The surface

679 daytime pollutant estimations with finer resolutions in space and time based on a unified

680 modeling framework will offer an unprecedented view to characterize the near-surface

681 O_3 formation regimes. Notwithstanding the relatively limited duration of the study, this

682 work offers valuable insights into the current state and causes of urban-nonurban

683 disparities in O_3 pollution. Future efforts should conduct a more detailed long-term

684 evaluation of urban-nonurban disparities in global O_3 levels and the impact of formation

685 mechanisms to further our understanding of air pollution and its mitigation.

Competing Interests

687 The authors declare that they have no conflict of interest.

Acknowledgments

689 The work was financially supported by the National Natural Science Foundation

690 of China (project No. 22236004) and Taishan Scholars (No. ts201712003).

Code and Data Availability

692 The Air Transformer deep learning framework is available on GitHub

693 (https://github.com/myles-tcl/Air-Transformer), which provides the scripts for

694 spatiotemporal data extraction, normalization, model training, and estimating of multi-

695 pollutants. The sources of input data in the Air Transformer can be found in Table S1.

696 The estimation of the Air Transformer can be downloaded from Zenodo:

697 https://zenodo.org/records/10071408 (Tao, 2023).

Author Contributions

698

699   CT: Methodology, Software, Validation, Formal analysis, Investigation, Data

700 Curation, Writing-Original Draft, Visualization. YP: Conceptualization, Writing-

701 Review & Editing. QZ: Writing-Review & Editing, Project administration, Funding

702 acquisition. YZ: Methodology, Writing-Review & Editing. BG: Software, Writing-

703 Review & Editing. QW: Supervision, Writing-Review & Editing. WW: Supervision,

704 Writing-Review & Editing.

705

References

706 **References**

707 Bertasius, G., Wang, H., and Torresani, L.: Is Space-Time Attention All You Need for

708   Video Understanding?, http://arxiv.org/abs/2102.05095, 9 June 2021.

709 Chen, T. and Guestrin, C.: XGBoost: A Scalable Tree Boosting System, in: Proceedings

710   of the 22nd ACM SIGKDD International Conference on Knowledge Discovery

711   and Data Mining, KDD'16: The 22nd ACM SIGKDD International Conference

712   on Knowledge Discovery and Data Mining, San Francisco California USA, 785–

713   794, https://doi.org/10/gdp84q, 2016.

714 Action Plan on Air Pollution Prevention and Control (in Chinese):

715   http://www.gov.cn/zwgk/2013-09/12/content_2486773.htm, last access: 1

716   February 2023.

717 Chu, W., Li, H., Ji, Y., Zhang, X., Xue, L., Gao, J., and An, C.: Research on ozone

718   formation sensitivity based on observational methods: Development history,

719   methodology, and application and prospects in China, Journal of Environmental

720   Sciences, S1001074223000980, https://doi.org/10/gr4qzk, 2023.

721 Cooper, M. J., Martin, R. V., Hammer, M. S., Levelt, P. F., Veefkind, P., Lamsal, L. N.,

722   Krotkov, N. A., Brook, J. R., and McLinden, C. A.: Global fine-scale changes in

723   ambient NO_2 during COVID-19 lockdowns, Nature, 601, 380–387,

724   https://doi.org/10.1038/s41586-021-04229-0, 2022.

725 Copernicus Sentinel-5P (processed by ESA): TROPOMI Level 2 Ozone Total Column

726   products (Version 02), https://doi.org/10.5270/S5P-ft13p57, 2020.

727 Di, Q., Kloog, I., Koutrakis, P., Lyapustin, A., Wang, Y., and Schwartz, J.: Assessing

728    $PM_{2.5}$ Exposures with High Spatiotemporal Resolution across the Continental

729   United States, Environ. Sci. Technol., 50, 4712–4721,

730   https://doi.org/10.1021/acs.est.5b06121, 2016.

731 Dias, D. and Tchepel, O.: Spatial and Temporal Dynamics in Air Pollution Exposure

732   Assessment, IJERPH, 15, 558, https://doi.org/10.3390/ijerph15030558, 2018.

733 Didan, K.: MODIS/Terra Vegetation Indices 16-Day L3 Global 250m SIN Grid V061,

NASA EOSDIS Land Processes Distributed Active Archive Center, https://doi.org/10.5067/MODIS/MOD13Q1.061, 2021.

van Donkelaar, A., Martin, R. V., Spurr, R. J. D., and Burnett, R. T.: High-Resolution Satellite-Derived $PM_{2.5}$ from Optimal Estimation and Geographically Weighted Regression over North America, Environ. Sci. Technol., 49, 10482–10491, https://doi.org/10.1021/acs.est.5b02076, 2015.

Dosovitskiy, A., Beyer, L., Kolesnikov, A., Weissenborn, D., Zhai, X., Unterthiner, T., Dehghani, M., Minderer, M., Heigold, G., Gelly, S., Uszkoreit, J., and Houlsby, N.: An Image is Worth 16x16 Words: Transformers for Image Recognition at Scale, https://doi.org/10.48550/arXiv.2010.11929, 3 June 2021.

Dyson, J. E., Whalley, L. K., Slater, E. J., Woodward-Massey, R., Ye, C., Lee, J. D., Squires, F., Hopkins, J. R., Dunmore, R. E., Shaw, M., Hamilton, J. F., Lewis, A. C., Worrall, S. D., Bacak, A., Mehra, A., Bannan, T. J., Coe, H., Percival, C. J., Ouyang, B., Hewitt, C. N., Jones, R. L., Crilley, L. R., Kramer, L. J., Acton, W. J. F., Bloss, W. J., Saksakulkrai, S., Xu, J., Shi, Z., Harrison, R. M., Kotthaus, S., Grimmond, S., Sun, Y., Xu, W., Yue, S., Wei, L., Fu, P., Wang, X., Arnold, S. R., and Heard, D. E.: Impact of HO_2 aerosol uptake on radical levels and O_3 production during summertime in Beijing, Atmos. Chem. Phys., 23, 5679–5697, https://doi.org/10/gshrst, 2023.

Geng, G., Xiao, Q., Liu, S., Liu, X., Cheng, J., Zheng, Y., Xue, T., Tong, D., Zheng, B., Peng, Y., Huang, X., He, K., and Zhang, Q.: Tracking Air Pollution in China: Near Real-Time $PM_{2.5}$ Retrievals from Multisource Data Fusion, Environ. Sci. Technol., 55, 12106–12115, https://doi.org/10.1021/acs.est.1c01863, 2021.

Global Modeling and Assimilation Office (GMAO): MERRA-2 inst3_2d_gas_Nx: 2d, 3-Hourly, Instantaneous, Single-Level, Assimilation, Aerosol Optical Depth Analysis V5.12.4, Greenbelt, MD, USA, Goddard Earth Sciences Data and Information Services Center (GES DISC), https://doi.org/10.5067/HNGA0EWW0R09, 2015.

Han, H., Zhang, L., Liu, Z., Yue, X., Shu, L., Wang, X., and Zhang, Y.: Narrowing Differences in Urban and Nonurban Surface Ozone in the Northern Hemisphere Over 1990–2020, Environ. Sci. Technol. Lett., 10, 410–417, https://doi.org/10/gsd5gk, 2023.

Han, X. and Naeher, L. P.: A review of traffic-related air pollution exposure assessment studies in the developing world, Environment International, 32, 106–120, https://doi.org/10.1016/j.envint.2005.05.020, 2006.

Hersbach, H., Bell, B., Berrisford, G., Horányi, A., Muñoz Sabater, J., Nicolas, J., Peubey, C., Rozum, I., Schepers, D., Simmons, A., Soci, C., Dee, D., and Thépaut, J.-N.: ERA5 hourly data on single levels from 1959 to present, Copernicus Climate Change Service (C3S) Climate Data Store (CDS), https://doi.org/10.24381/cds.adbb2d47, 2023.

Huang, C., Hu, J., Xue, T., Xu, H., and Wang, M.: High-Resolution Spatiotemporal Modeling for Ambient $PM_{2.5}$ Exposure Assessment in China from 2013 to 2019, Environ. Sci. Technol., 55, 2152–2162, https://doi.org/10.1021/acs.est.0c05815, 2021.

Inness, A., Ades, M., Agustí-Panareda, A., Barré, J., Benedictow, A., Blechschmidt, A.-M., Dominguez, J. J., Engelen, R., Eskes, H., Flemming, J., Huijnen, V., Jones, L., Kipling, Z., Massart, S., Parrington, M., Peuch, V.-H., Razinger, M., Remy, S., Schulz, M., and Suttie, M.: The CAMS reanalysis of atmospheric composition, Atmos. Chem. Phys., 19, 3515–3556, https://doi.org/10/ghdkrm, 2019.

Ivatt, P. D., Evans, M. J., and Lewis, A. C.: Suppression of surface ozone by an aerosol-inhibited photochemical ozone regime, Nat. Geosci., 15, 536–540, https://doi.org/10.1038/s41561-022-00972-9, 2022.

Jerrett, M., Arain, A., Kanaroglou, P., Beckerman, B., Potoglou, D., Sahsuvaroglu, T., Morrison, J., and Giovis, C.: A review and evaluation of intraurban air pollution exposure models, Journal of Exposure Science & Environmental Epidemiology, 15, 185–204, https://doi.org/10.1038/sj.jea.7500388, 2005.

790 Jin, X., Fiore, A. M., Murray, L. T., Valin, L. C., Lamsal, L. N., Duncan, B., Folkert

791   Boersma, K., De Smedt, I., Abad, G. G., Chance, K., and Tonnesen, G. S.:

792   Evaluating a Space-Based Indicator of Surface Ozone-NO_x-VOC Sensitivity Over

793   Midlatitude Source Regions and Application to Decadal Trends: Space-Based

794   Indicator of O_3 Sensitivity, J. Geophys. Res. Atmos., 122, 10,439-10,461,

795   https://doi.org/10.1002/2017JD026720, 2017.

796 Jin, X., Fiore, A., Boersma, K. F., Smedt, I. D., and Valin, L.: Inferring Changes in

797   Summertime Surface Ozone-NO_x-VOC Chemistry over U.S. Urban Areas from

798   Two Decades of Satellite and Ground-Based Observations, Environ. Sci. Technol.,

799   54, 6518–6529, https://doi.org/10.1021/acs.est.9b07785, 2020.

800 Jin, X., Fiore, A. M., and Cohen, R. C.: Space-Based Observations of Ozone Precursors

801   within California Wildfire Plumes and the Impacts on Ozone-NO_x-VOC

802   Chemistry, Environ. Sci. Technol., 57, 14648–14660,

803   https://doi.org/10.1021/acs.est.3c04411, 2023.

804 Jun, C., Ban, Y., and Li, S.: China: Open access to Earth land-cover map, Nature, 514,

805   434–434, https://doi.org/DOI:10.1038/514434c, 2014.

806 Jung, J., Choi, Y., Souri, A. H., Mousavinezhad, S., Sayeed, A., and Lee, K.: The Impact

807   of Springtime-Transported Air Pollutants on Local Air Quality With Satellite-

808   Constrained NO_x Emission Adjustments Over East Asia, Journal of Geophysical

809   Research: Atmospheres, 127, e2021JD035251,

810   https://doi.org/10.1029/2021JD035251, 2022.

811 Ke, G., Meng, Q., Finley, T., Wang, T., Chen, W., Ma, W., Ye, Q., and Liu, T.-Y.:

812   LightGBM: A Highly Efficient Gradient Boosting Decision Tree, in: Proceedings

813   of the 31st International Conference on Neural Information Processing Systems,

814   Red Hook, NY, USA, event-place: Long Beach, California, USA, 3149–3157,

815   2017.

816 Kohno, N., Zhou, J., Li, J., Takemura, M., Ono, N., Sadanaga, Y., Nakashima, Y., Sato,

817   K., Kato, S., Sakamoto, Y., and Kajii, Y.: Impacts of missing OH reactivity and

aerosol uptake of HO$_2$ radicals on tropospheric O$_3$ production during the AQUAS-Kyoto summer campaign in 2018, Atmospheric Environment, 281, 119130, https://doi.org/10/gshfc4, 2022.

Lamsal, L. N., Krotkov, N. A., Marchenko, S. V., Joiner, J., Oman, L., Vasilkov, A., Fisher, B., Qin, W., Yang, E.-S., Fasnacht, Z., Choi, S., Leonard, P., and Haffner, D.: TROPOMI/S5P NO$_2$ Tropospheric, Stratospheric and Total Columns MINDS 1-Orbit L2 Swath 5.5 km x 3.5 km, Goddard Earth Sciences Data and Information Services Center (GES DISC), https://doi.org/10.5067/MEASURES/MINDS/DATA203, 2022.

Lee, H. J., Kuwayama, T., and FitzGibbon, M.: Trends of ambient O$_3$ levels associated with O$_3$ precursor gases and meteorology in California: Synergies from ground and satellite observations, Remote Sensing of Environment, 284, 113358, https://doi.org/10.1016/j.rse.2022.113358, 2023.

Li, C., Zhu, Q., Jin, X., and Cohen, R. C.: Elucidating Contributions of Anthropogenic Volatile Organic Compounds and Particulate Matter to Ozone Trends over China, Environ. Sci. Technol., 56, 12906–12916, https://doi.org/10.1021/acs.est.2c03315, 2022a.

Li, D., Wang, S., Xue, R., Zhu, J., Zhang, S., Sun, Z., and Zhou, B.: OMI-observed HCHO in Shanghai, China, during 2010–2019 and ozone sensitivity inferred by an improved HCHO / NO$_2$ ratio, Atmos. Chem. Phys., 21, 15447–15460, https://doi.org/10.5194/acp-21-15447-2021, 2021a.

Li, K., Jacob, D. J., Liao, H., Zhu, J., Shah, V., Shen, L., Bates, K. H., Zhang, Q., and Zhai, S.: A two-pollutant strategy for improving ozone and particulate air quality in China, Nat. Geosci., 12, 906–910, https://doi.org/10.1038/s41561-019-0464-x, 2019.

Li, K., Wang, Y., Peng, G., Song, G., Liu, Y., Li, H., and Qiao, Y.: UniFormer: Unified Transformer for Efficient Spatial-Temporal Representation Learning, International Conference on Learning Representations, 2021b.

846 Li, L. and Wu, J.: Spatiotemporal estimation of satellite-borne and ground-level NO_2

847   using full residual deep networks, Remote Sensing of Environment, 254, 112257,

848   https://doi.org/10.1016/j.rse.2020.112257, 2021.

849 Li, M., Wang, T., Xie, M., Zhuang, B., Li, S., Han, Y., and Chen, P.: Impacts of aerosol-

850   radiation feedback on local air quality during a severe haze episode in Nanjing

851   megacity, eastern China, Tellus B: Chemical and Physical Meteorology, 69,

852   1339548, https://doi.org/10/gsfjz3, 2017.

853 Li, M., Yang, Q., Yuan, Q., and Zhu, L.: Estimation of high spatial resolution ground-

854   level ozone concentrations based on Landsat 8 TIR bands with deep forest model,

855   Chemosphere, 301, 134817, https://doi.org/10.1016/j.chemosphere.2022.134817,

856   2022b.

857 Lin, C., Huang, R.-J., Zhong, H., Duan, J., Wang, Z., Huang, W., and Xu, W.:

858   Elucidating ozone and PM $_{2.5}$ pollution in the Fenwei Plain reveals the co-benefits

859   of controlling precursor gas emissions in winter haze, Atmos. Chem. Phys., 23,

860   3595–3607, https://doi.org/10/gsfvs3, 2023.

861 Liu, M., Huang, Y., Ma, Z., Jin, Z., Liu, X., Wang, H., Liu, Y., Wang, J., Jantunen, M.,

862   Bi, J., and Kinney, P. L.: Spatial and temporal trends in the mortality burden of air

863   pollution in China: 2004–2012, Environment International, 98, 75–81,

864   https://doi.org/10.1016/j.envint.2016.10.003, 2017.

865 Liu, X., Shi, X., Lei, Y., and Xue, W.: Path of coordinated control of $PM_{2.5}$ and ozone

866   in China, Chin. Sci. Bull., 67, 2089–2099, https://doi.org/10.1360/TB-2021-0832,

867   2022.

868 Lu, D., Mao, W., Zheng, L., Xiao, W., Zhang, L., and Wei, J.: Ambient $PM_{2.5}$ Estimates

869   and Variations during COVID-19 Pandemic in the Yangtze River Delta Using

870   Machine Learning and Big Data, Remote Sensing, 13, 1423,

871   https://doi.org/10.3390/rs13081423, 2021.

872 Lu, X., Hong, J., Zhang, L., Cooper, O. R., Schultz, M. G., Xu, X., Wang, T., Gao, M.,

873   Zhao, Y., and Zhang, Y.: Severe Surface Ozone Pollution in China: A Global

874   Perspective, Environ. Sci. Technol. Lett., 5, 487–494,
875   https://doi.org/10.1021/acs.estlett.8b00366, 2018.

876 Lundberg, S. M. and Lee, S.-I.: A Unified Approach to Interpreting Model Predictions,
877   in: Proceedings of the 31st International Conference on Neural Information
878   Processing Systems, Red Hook, NY, USA, 2017.

879 Lyapustin, A. and Wang, Y.: MODIS/Terra+Aqua Land Aerosol Optical Depth Daily
880   L2G Global 1km SIN Grid V061, NASA EOSDIS Land Processes DAAC,
881   https://doi.org/10.5067/MODIS/MCD19A2.061, 2022.

882 Miller, D. F., Alkezweeny, A. J., Hales, J. M., and Lee, R. N.: Ozone Formation Related
883   to Power Plant Emissions, Science, 202, 1186–1188, https://doi.org/10/b5kgjr,
884   1978.

885 Mitchell, R., Frank, E., and Holmes, G.: GPUTreeShap: massively parallel exact
886   calculation of SHAP scores for tree ensembles, PeerJ Computer Science, 8,
887   https://doi.org/10.7717/peerj-cs.880, 2020.

888 Myers, S. L.: The Worst Dust Storm in a Decade Shrouds Beijing and Northern China,
889   The New York Times, 15th March, 2021.

890 Pusede, S. E., Steiner, A. L., and Cohen, R. C.: Temperature and Recent Trends in the
891   Chemistry of Continental Surface Ozone, Chem. Rev., 115, 3898–3918,
892   https://doi.org/10.1021/cr5006815, 2015.

893 Ren, J., Guo, F., and Xie, S.: Diagnosing ozone-NO_x-VOC sensitivity and revealing
894   causes of ozone increases in China based on 2013-2021 satellite retrievals, Atmos.
895   Chem. Phys., 22, 15035–15047, https://doi.org/10.5194/acp-22-15035-2022,
896   2022a.

897 Ren, X., Mi, Z., Cai, T., Nolte, C. G., and Georgopoulos, P. G.: Flexible Bayesian
898   Ensemble Machine Learning Framework for Predicting Local Ozone
899   Concentrations, Environ. Sci. Technol., 56, 3871–3883,
900   https://doi.org/10.1021/acs.est.1c04076, 2022b.

901 Requia, W. J., Di, Q., Silvern, R., Kelly, J. T., Koutrakis, P., Mickley, L. J., Sulprizio,

M. P., Amini, H., Shi, L., and Schwartz, J.: An Ensemble Learning Approach for Estimating High Spatiotemporal Resolution of Ground-Level Ozone in the Contiguous United States, Environ. Sci. Technol., 54, 11037–11047, https://doi.org/10.1021/acs.est.0c01791, 2020.

Román, M. O., Wang, Z., Sun, Q., Kalb, V., Miller, S. D., Molthan, A., Schultz, L., Bell, J., Stokes, E. C., Pandey, B., Seto, K. C., Hall, D., Oda, T., Wolfe, R. E., Lin, G., Golpayegani, N., Devadiga, S., Davidson, C., Sarkar, S., Praderas, C., Schmaltz, J., Boller, R., Stevens, J., Ramos González, O. M., Padilla, E., Alonso, J., Detrés, Y., Armstrong, R., Miranda, I., Conte, Y., Marrero, N., MacManus, K., Esch, T., and Masuoka, E. J.: NASA's Black Marble nighttime lights product suite, Remote Sensing of Environment, 210, 113–143, https://doi.org/10/ghqpjh, 2018.

Shapley, L. S.: A value for n-person games, in: The Shapley Value: Essays in Honor of Lloyd S. Shapley, edited by: Roth, A. E., Cambridge University Press, Cambridge, 31–40, https://doi.org/10.1017/CBO9780511528446.003, 1988.

Shrikumar, A., Greenside, P., and Kundaje, A.: Learning Important Features Through Propagating Activation Differences, http://arxiv.org/abs/1704.02685, 12 October 2019.

Sicard, P., Serra, R., and Rossello, P.: Spatiotemporal trends in ground-level ozone concentrations and metrics in France over the time period 1999–2012, Environmental Research, 149, 122–144, https://doi.org/10.1016/j.envres.2016.05.014, 2016.

Sicard, P., De Marco, A., Agathokleous, E., Feng, Z., Xu, X., Paoletti, E., Rodriguez, J. J. D., and Calatayud, V.: Amplified ozone pollution in cities during the COVID-19 lockdown, Science of The Total Environment, 735, 139542, https://doi.org/10/gg5w8h, 2020.

Sillman, S.: The use of NO_y, H_2O_2, and HNO_3 as indicators for ozone-NO_x-hydrocarbon sensitivity in urban locations, J. Geophys. Res., 100, 14175, https://doi.org/10.1029/94JD02953, 1995.

Song, H., Lu, K., Dong, H., Tan, Z., Chen, S., Zeng, L., and Zhang, Y.: Reduced Aerosol Uptake of Hydroperoxyl Radical May Increase the Sensitivity of Ozone Production to Volatile Organic Compounds, Environ. Sci. Technol. Lett., 9, 22–29, https://doi.org/10/gnqqb9, 2022a.

Song, K., Liu, R., Wang, Y., Liu, T., Wei, L., Wu, Y., Zheng, J., Wang, B., and Liu, S. C.: Observation-based analysis of ozone production sensitivity for two persistent ozone episodes in Guangdong, China, Atmos. Chem. Phys., 22, 8403–8416, https://doi.org/10/gr4qz2, 2022b.

Souri, A. H., Johnson, M. S., Wolfe, G. M., Crawford, J. H., Fried, A., Wisthaler, A., Brune, W. H., Blake, D. R., Weinheimer, A. J., Verhoelst, T., Compernolle, S., Pinardi, G., Vigouroux, C., Langerock, B., Choi, S., Lamsal, L., Zhu, L., Sun, S., Cohen, R. C., Min, K.-E., Cho, C., Philip, S., Liu, X., and Chance, K.: Characterization of errors in satellite-based HCHO∕NO$_2$ tropospheric column ratios with respect to chemistry, column-to-PBL translation, spatial representation, and retrieval uncertainties, Atmospheric Chemistry and Physics, 23, 1963–1986, https://doi.org/10.5194/acp-23-1963-2023, 2023.

Su, W., Hu, Q., Chen, Y., Lin, J., Zhang, C., and Liu, C.: Inferring global surface HCHO concentrations from multisource hyperspectral satellites and their application to HCHO-related global cancer burden estimation, Environment International, 170, 107600, https://doi.org/10.1016/j.envint.2022.107600, 2022.

Sun, H., Shin, Y. M., Xia, M., Ke, S., Wan, M., Yuan, L., Guo, Y., and Archibald, A. T.: Spatial Resolved Surface Ozone with Urban and Rural Differentiation during 1990–2019: A Space–Time Bayesian Neural Network Downscaler, Environ. Sci. Technol., 56, 7337–7349, https://doi.org/10.1021/acs.est.1c04797, 2022.

Tan, Z., Lu, K., Ma, X., Chen, S., He, L., Huang, X., Li, X., Lin, X., Tang, M., Yu, D., Wahner, A., and Zhang, Y.: Multiple Impacts of Aerosols on O$_3$ Production Are Largely Compensated: A Case Study Shenzhen, China, Environ. Sci. Technol., 56, 17569–17580, https://doi.org/10/gsgp79, 2022.

958   Tang, L., Xue, X., Qu, J., Mi, Z., Bo, X., Chang, X., Wang, S., Li, S., Cui, W., and Dong,

959   G.: Air pollution emissions from Chinese power plants based on the continuous

960   emission monitoring systems network, Sci Data, 7, 325, https://doi.org/10/ghfqqf,

961   2020.

962   Tao, C.: Surface Ozone, NO_2, and $PM_{2.5}$ Concentrations Estimated by the Deep

963   Learning model (Air Transformer) based on Satellite data,

964   https://doi.org/10.5281/zenodo.10071408, 2023.

965   Thongthammachart, T., Araki, S., Shimadera, H., Matsuo, T., and Kondo, A.:

966   Incorporating Light Gradient Boosting Machine to land use regression model for

967   estimating NO_2 and $PM_{2.5}$ levels in Kansai region, Japan, Environmental

968   Modelling & Software, 155, 105447,

969   https://doi.org/10.1016/j.envsoft.2022.105447, 2022.

970   Wei, J., Li, Z., Li, K., Dickerson, R. R., Pinker, R. T., Wang, J., Liu, X., Sun, L., Xue,

971   W., and Cribb, M.: Full-coverage mapping and spatiotemporal variations of

972   ground-level ozone (O_3) pollution from 2013 to 2020 across China, Remote

973   Sensing of Environment, 270, 112775, https://doi.org/10.1016/j.rse.2021.112775,

974   2022a.

975   Wei, J., Liu, S., Li, Z., Liu, C., Qin, K., Liu, X., Pinker, R. T., Dickerson, R. R., Lin, J.,

976   Boersma, K. F., Sun, L., Li, R., Xue, W., Cui, Y., Zhang, C., and Wang, J.: Ground-

977   Level NO_2 Surveillance from Space Across China for High Resolution Using

978   Interpretable Spatiotemporally Weighted Artificial Intelligence, Environ. Sci.

979   Technol., acs.est.2c03834, https://doi.org/10.1021/acs.est.2c03834, 2022b.

980   Wei, W., Wang, X., Wang, X., Li, R., Zhou, C., and Cheng, S.: Attenuated sensitivity of

981   ozone to precursors in Beijing–Tianjin–Hebei region with the continuous NOx

982   reduction within 2014–2018, Science of The Total Environment, 813, 152589,

983   https://doi.org/10/gq7ngn, 2022c.

984   WorldPop: Global High Resolution Population Denominators Project - Funded by The

985   Bill and Melinda Gates Foundation (OPP1134076).,

986 https://dx.doi.org/10.5258/SOTON/WP00675, 2018.

987 Xiao, Q., Chang, H. H., Geng, G., and Liu, Y.: An Ensemble Machine-Learning Model

988  To Predict Historical $PM_{2.5}$ Concentrations in China from Satellite Data, Environ.

989  Sci. Technol., 52, 13260–13269, https://doi.org/10.1021/acs.est.8b02917, 2018.

990 Yue, X., Unger, N., Harper, K., Xia, X., Liao, H., Zhu, T., Xiao, J., Feng, Z., and Li, J.:

991  Ozone and haze pollution weakens net primary productivity in China,

992  Atmospheric Chemistry and Physics, 17, 6073–6089, https://doi.org/10.5194/acp-

993  17-6073-2017, 2017.

994 Zhang, J., Wang, J., Sun, Y., Li, J., Ninneman, M., Ye, J., Li, K., Crandall, B., Mao, J.,

995  Xu, W., Schwab, M. J., Li, W., Ge, X., Chen, M., Ying, Q., Zhang, Q., and Schwab,

996  J. J.: Insights from ozone and particulate matter pollution control in New York City

997  applied to Beijing, npj Clim Atmos Sci, 5, 85, https://doi.org/10.1038/s41612-022-

998  00309-8, 2022.

999 Zhang, R., Lei, W., Tie, X., and Hess, P.: Industrial emissions cause extreme urban

1000  ozone diurnal variability, Proc. Natl. Acad. Sci. U.S.A., 101, 6346–6350,

1001  https://doi.org/10.1073/pnas.0401484101, 2004.

1002 Zhao, M., Cheng, C., Zhou, Y., Li, X., Shen, S., and Song, C.: A global dataset of annual

1003  urban extents (1992–2020) from harmonized nighttime lights, Earth System

1004  Science Data, 14, 517–534, https://doi.org/10.5194/essd-14-517-2022, 2022.

1005 Zheng, B., Tong, D., Li, M., Liu, F., Hong, C., Geng, G., Li, H., Li, X., Peng, L., Qi, J.,

1006  Yan, L., Zhang, Y., Zhao, H., Zheng, Y., He, K., and Zhang, Q.: Trends in China's

1007  anthropogenic emissions since 2010 as the consequence of clean air actions,

1008  Atmos. Chem. Phys., 18, 14095–14111, https://doi.org/10.5194/acp-18-14095-

1009  2018, 2018.

1010